

## STELLAR METALLICITY GRADIENTS IN SDSS GALAXIES

BENJAMIN ROIG<sup>1</sup>, MICHAEL R. BLANTON<sup>1</sup>, RENBIN YAN<sup>2</sup>  
*Draft version June 19, 2018*

### ABSTRACT

We infer stellar metallicity and abundance ratio gradients for a sample of red galaxies in the Sloan Digital Sky Survey (SDSS) Main galaxy sample. Because this sample does not have multiple spectra at various radii in a single galaxy, we measure these gradients statistically. We separate galaxies into stellar mass bins, stack their spectra in redshift bins, and calculate the measured absorption line indices in projected annuli by differencing spectra in neighboring redshift bins. After determining the line indices, we use stellar population modeling from the EZ\_Ages software to calculate ages, metallicities, and abundance ratios within each annulus. Our data covers the central regions of these galaxies, out to slightly higher than  $1R_e$ . We find detectable gradients in metallicity and relatively shallow gradients in abundance ratios, similar to results found for direct measurements of individual galaxies. The gradients are only weakly dependent on stellar mass, and this dependence is well-correlated with the change of  $R_e$  with mass. Based on this data, we report mean equivalent widths, metallicities, and abundance ratios as a function of mass and velocity dispersion for SDSS early-type galaxies, for fixed apertures of 2.5 kpc and of  $0.5 R_e$ .

### 1. INTRODUCTION

The study of stellar population and metallicity gradients has been an ongoing topic because it places relatively strong constraints on the evolutionary history of galaxies. This has been a much-studied field for the past 50-60 years, with a wealth of information available that allows the interpretation of galaxy spectra in terms of stellar populations (Faber et al. 1985 for example). Early studies that correlated observable metal absorption lines with stellar population properties only could examine small numbers of galaxies (e.g. Couture & Hardy 1988; Munn 1992; Gonzalez & Gorgas 1995), but led to the acceptance that galaxies typically had lower metallicities at larger radii. Later studies have increased the sample size, measured additional metal absorption indices, and added detail to that basic picture (Carollo et al. 1993; Koleva et al. 2011).

Theoretical studies have also, of course, addressed the question of what causes this common trend in elliptical galaxies (Martinelli et al. 1998; Ogando et al. 2006 are several of many). Mergers, star formation histories, gas flow, and other mechanisms help determine the metallicity gradients. Mergers can drastically change the distribution of stars in the final galaxies, affecting the observed metallicity gradients dramatically as well (Di Matteo et al. 2009). Conversely, a lack of mergers can lead to the evolution of a metallicity gradient after the infall of cooling gas (Pipino et al. 2010). Predicting the observed stellar metallicity gradients correctly requires a model of the star formation and formation history (mergers or otherwise) of galaxies. This suggests that a large-scale study of metallicity gradients in elliptical galaxies may help our understanding of the average path an elliptical galaxy takes in formation — how many mergers, mass ratios of the mergers, when star formation

bursts occur, and how long these formation bursts last, among other properties.

Equally, observing metallicity gradients in a large sample of galaxies has been a challenge, as it requires spectra of multiple regions of the same galaxy. Usually, then, observational studies that attempt to constrain theoretical models are restricted to a relatively small number of nearby galaxies (Greene et al. 2013; Spolaor et al. 2010; Kuntschner et al. 2010; Rawle et al. 2010; Pastorello et al. 2014), which makes them sensitive to the specific choice of galaxies to observe. Newer projects (including González Delgado et al. (2014) with the CALIFA survey and Bundy et al. (2015) with MaNGA) study these gradients using integral field spectroscopy (IFS) to attempt to improve our understanding. Here, we study a large number of galaxies observed by the Sloan Digital Sky Survey (SDSS) and instead of finding metallicity gradients in individual galaxies, we average galaxies in redshift bins and calculate statistical gradients between annuli found by subtracting galaxy fluxes at different redshifts from each other. This process yields the population-averaged metallicity and abundance profiles of early type galaxies.

We begin by selecting a sample of non-starforming galaxies in SDSS, as detailed in Section 2. We measure the standard Lick indices used to calculate age and metallicity, and make use of EZ\_AGES (Graves & Schiavon 2008) to obtain those parameters. With our sample complete, we compare our calculated gradients to several other studies in Section 6 to verify the accuracy of our approach, focusing on studies that also are able to find gradients in the inner  $1R_e$  of galaxies rather than ones that examine the full outer regions as well. We then examine several papers that discuss theoretical models for the formation of these galaxies to see which our observations support and what, if any, conclusions we can draw about likely evolutionary histories of our galaxies in Section 7.

<sup>1</sup> Center for Cosmology and Particle Physics, Department of Physics, New York University, 4 Washington Place, New York, NY 10003

<sup>2</sup> University of Kentucky

### 2. SAMPLE SELECTION

Our sample is composed of a subset of the NYU Value-Added Galaxy Catalog (NYU-VAGC; Blanton et al. 2005), based on the SDSS Data Release 7 (DR7; Abazajian et al. 2009). We use 686,356 Main sample galaxies (Strauss et al. 2002) with observed spectra and several extracted values from the observations (redshift, a half-light radius, magnitudes in several bands, and an estimate of the stellar mass). The stellar mass we use is estimated from the K-corrected mass-to-light ratios in the *ugriz* and JHK bands (see Blanton & Roweis 2007 for details).

We wish to select a uniform sample of non-starforming galaxies so that we can have confidence that the properties remain relatively the same across the entire redshift range of our study and avoid any emission line contamination of the features we seek to measure. To do this, we perform a few simple cuts involving [OII] and  $H\alpha$  equivalent widths (EWs) as previously done in Yan et al. (2006) that yield cuts in spectroscopic properties. First, objects that have [OII] emission but no  $H\alpha$  are kept in the sample. Second, any object without either [OII] or  $H\alpha$  emission is kept. Finally, for objects with both [OII] and  $H\alpha$ , we keep ones with a high ratio of [OII]/ $H\alpha$  and reject those with a low ratio. We define this ratio as Yan et al. (2006) does ( $EW([OII]) > 5EW(H\alpha) - 7$ ) and we keep all objects that pass this ratio of those with both lines detected. These cuts may potentially exclude some red, non-starforming galaxies as the cost of being sure the number of blue, starforming galaxies remaining in the sample is very low (approximately 3% per Yan et al. 2006). We do not, however, make any morphology cuts; this suggests about 40% of the sample will be pure elliptical galaxies, with the rest a mix of S0 or Sa morphologies (Blanton & Moustakas 2009). The dependence of gradients on a mix of E, S0, and Sa morphologies has been found to have limited effect (see González Delgado et al. 2014, Fig. 5), so this may not dramatically impact our results, but should be remembered as a caveat.

This leaves us with 266,195 non-starforming galaxies to work with. The next set of cuts is to ensure that the data remaining has correctly measured results for all the important parameters that we will need. We remove all objects with masses less than  $10^7$  and all objects that do not have measured EWs for the metal indices (Mg b, Fe5270, Fe5335, Ca4227, and C4668) that we will be using, as well as  $H\beta$ , which tends to happen only in the rare case of a badly fit absorption line. This is a relatively minor adjustment and only reduces our sample by approximately 4%.

Finally, metallicities are dependent on the stellar masses of the galaxies, and so we break up the data into mass bins, each individually volume limited, the details of which are given in Table 1. We have also alternatively divided the galaxies into velocity dispersion bins, with the name number of bins and volume limiting cuts in redshift and magnitude.

As a note, the mass bins are large enough to still leave around a factor of two difference in the brightest versus dimmest galaxies in each bin; however, in tests to see if this luminosity range overly weighted the brightest galaxies in each bin in measuring line fluxes we found less than a 5% steepening of the indicator gradients when normalizing luminosities versus leaving them unchanged. For the results presented in this paper, we do not normalize

TABLE 1  
VOLUME LIMITED MASS BINNING OF GALAXIES IN THIS PAPER

$\log(M)$ Range	$z$ Range	Max V Mag	Objects
$10.0 < \log M < 10.3$	$0.02 < z < 0.09$	-19.35	23324
$10.3 < \log M < 10.7$	$0.02 < z < 0.12$	-20.05	57381
$10.7 < \log M < 11.0$	$0.03 < z < 0.18$	-21.05	50880
$11.0 < \log M < 11.5$	$0.07 < z < 0.24$	-21.80	22029

NOTE. — 4 stellar mass bins are chosen for the galaxies in this paper to reduce the effects of the mass dependence of metallicity. Each bin has a redshift range and magnitude limit selected to maximize the number of objects in the sample while ensuring that the sample remains volume limited.

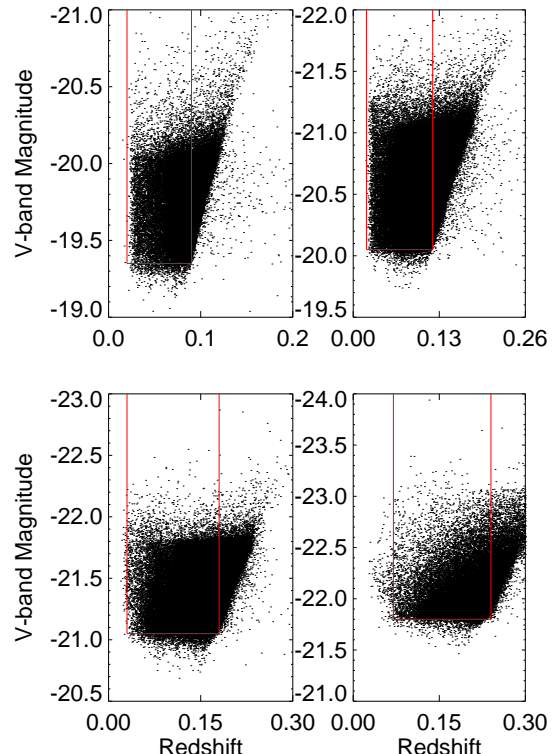


FIG. 1.— The cuts made to create a volume-limited sample for each stellar mass bin.

each galaxy in a mass bin to the same luminosity, but rather leave the luminosities as they are for each individual galaxy.

Figure 1 shows the resulting samples with the cuts in red lines.

In preparation for Lick index measurement, we must make two adjustments to our spectra. The first is a resolution correction — as Zhu et al. (2010) notes when performing the same corrections, SDSS spectra are not at the same resolution at which the originally defined Lick indices were observed. Schiavon (2007) contains several tables (Tables 43–46, depending on galaxy age) in which corrections for a given velocity dispersion to the Lick IDS resolution are defined, but to establish as common a baseline as we can between mass bins, we smooth all galaxies in our sample to the same velocity dispersion of  $325 \text{ km s}^{-1}$ . Any errors in the resolution correction from Schiavon (2007) will thus at least be the same for every galaxy, hopefully ensuring that any gradient trends we report will be independent of these errors. We use the table of corrections for a 7.9 Gyr population, noting

that while some of our galaxies will be older and some younger, the differences are only a few percent for corrections of a different stellar population age. The second correction, also defined by Schiavon (2007), is a fluxing correction to bring the SDSS spectra in line with the Lick IDS system. It too is empirical, with potentially large error, but we apply this correction after each Lick index is measured to fully bring our results in line with the Lick IDS system, noting unfortunately that errors from these corrections cannot be included in our error budget as well.

Each object that is kept in the sample then has its Lick indices for Mg b, Fe 5335, Fe 5270, Ca 4227, C 4668, and  $H\beta$  measured. In addition to the Lick index, we also measure the absorption line flux and continuum values directly over the same wavelength range. We also measure the [OIII] line flux to correct for  $H\beta$  line infill due to emission (see Zhu et al. 2010; Trager et al. 2000; Mehlert et al. 2000 for some discussion on the process and difficulties behind this correction). We use the standard correction factor of  $\Delta EW_{H\beta} = 0.6EW([OIII])$  that these prior works settle on with the understanding that it is empirical and has relatively large scatter, instead of attempting a correction where we would directly adjust the flux (instead of the equivalent width) of the  $H\beta$  absorption based on the measured flux of the [OIII] emission. In this [OIII] line fitting, we ignore any lines that are weak detections (defined as indistinguishable from zero line flux or EW at the one sigma level), and simply do not correct  $H\beta$  for those objects. We do have data for other commonly used indicators such as D4000 or CN1 and CN2, but the population modeling code we use does not use these as inputs to determine metallicity or age, so we do not present them here.

We convert several other of the above measured Lick indices to commonly used combinations in calculations of metallicity as well. First we compute  $[MgFe]' = \sqrt{Mgb \times (0.72Fe5270 + 0.28Fe5335)}$ , and secondly we compute  $\langle Fe \rangle = (Fe5270 + Fe5335)/2$ . Both these combinations are chosen because they more directly correlate with metallicity than any single Lick index (Thomas et al. 2003). This gives us 5 metallicity indicators ( $[MgFe]'$ ,  $\langle Fe \rangle$ , Mg b, Ca 4227, C 4668) and one age-related indicator (corrected  $H\beta$ ) for each of our galaxies that we will analyze.

### 3. MOCK CATALOG COMPARISON AND CORRECTION

To confirm that we can accurately measure gradients using this annulus method, we test the procedure on mock galaxy spectra generated with known metallicity gradients. To create this catalog, we use the NASA-Sloan Atlas (described in Blanton et al. 2011) as our reference for the properties of similar red and old galaxies. We apply the same selection criteria to the NASA-Sloan Atlas as in Section 2 to ensure we only have red galaxies, and then randomly select galaxies from the remaining catalog. We assign the Sersic index  $n$ , the Sersic half-light radius (in kpc), the absolute magnitude in the  $ugriz$  bands, the stellar mass, and the axis ratio  $b/a$  for each randomly chosen galaxy; we then assign a random redshift in our sample (0.02 to 0.24) to the galaxy. Based on this new redshift, we rescale the half-light radii into angular units and the luminosities into fluxes for each galaxy. We then perform the identical volume limiting

cuts based on redshift and V-band magnitude for each galaxy, creating a sample of red galaxies that would pass all our real samples cuts as well.

We next create mock spectra using Flexible Stellar Population Synthesis code (FSPS); (Conroy et al. 2009; Conroy & Gunn 2010), run via the Python-FSPS modules written by Daniel Foreman-Mackey, for a range of metallicities from 0.10 to  $-1.00$ , spaced at 0.01 dex, all with identical 10 Gyear ages. To properly create the mock spectra we would observe for a galaxy with a metallicity gradient, we create a pixel grid (resolution of 0.1 arcsec/pixel) where each pixels distance from the center determines its metallicity and therefore which FSPS-generated spectrum it is assigned. We generate the profile of our mock galaxies given their Sersic indices and radii and the axis ratio  $b/a$ , which lets us know the fraction of the luminosity coming from each pixel. We then assign a metallicity to each pixel based on its radial distance from the center by using a simple linear fit with constant and slope parameters chosen by us. The metallicity profile follows the light profile of the galaxy — steeper along the minor axis as defined by the  $b/a$  ratio of the galaxy.

Finally, we must generate a model for the aperture these galaxies are observed with. We convolve an image of the SDSS-I and -II fiber aperture (3 arcsecond diameter), placed at the exact center of each galaxy, with a double-Gaussian PSF. The Gaussians are both wavelength-dependent and variable across a range of possible seeings based on the actual BOSS seeing. For the core Gaussian, we define a mean FWHM of 1.5 arcseconds at 6000 angstroms, with variability around the mean of 0.3 arcseconds. The second Gaussian has a mean FWHM of 5.0 arcseconds at 6000 angstroms, also with variability around the mean of 0.3 arcseconds. For the wavelength dependence, we assume a  $\lambda^{-1/5}$  dependence for both Gaussians. The second Gaussian integral is weighted with a factor of 0.1 relative to the first.

With our aperture and galaxy image created, we then multiply the two together to model how much light at each pixel we would observe, and then weight the FSPS-generated spectrum of the metallicity of the pixel by that factor, finally summing all the pixels to generate a single mock spectrum that represents what we would observe for a galaxy with the metallicity gradient we have assigned.

We do not include noise in our procedure. Although noise in the spectra will cause noise in the result, it will not change the expectation value of the result; i.e. it will not change the expected slope of the measured profile.

Following this process, we create a mock catalog of 22,000 galaxies with known metallicity gradients to analyze identically to our real sample. We run it through the same procedures as for the real data to extract the metallicity indicators in each annulus for each mass bin and compare to the metallicity indicators we input at each radial point. The results of this are shown in Fig. 2. The black lines are the gradients in each indicator that were input, and the blue line shows what our annulus measuring code returns as outputs. We test a range of input metallicity gradients of similar magnitudes to our measured results to ensure that our method works for both steep and shallow gradients. We find that our

method leads to a slight constant offset from our inputs and a minor slope steepening (around 15–25%, depending on mass bin and indicator). However, the changes are not so dramatic as to invalidate the method. This steepening of the gradient likely occurs for two reasons: first, with an axis ratio not equal to one, our circular annuli are overlaid on elliptical constant-metallicity contours (based on the galaxy  $b/a$  axis ratio). This will cause some data from lower metallicities to be included. This lowers the indicator values. Secondly, the PSF we use smears light from the entire galaxy image into the aperture, albeit at a very low weighting on the low-metallicity edges. This, too, will lower the indicator values, but will have a greater impact at high redshift (larger effective aperture) due to the differences in how fast the PSF falls off away from the center (a Gaussian) and how fast the metallicity declines away from the center (log-linearly), resulting in a steepening gradient as well as a constant offset.

To examine these differences, we compare the measured Lick index values that we input to our recorded output values after the analysis, as shown in Fig. 2.

We find that our results are sensitive to the axis ratio distribution and the number of objects in each bin — a large percentage of objects in a bin with extreme axis ratios can cause large (and not real) scatter in the two annulus points calculated from that bin. We find it that this effect is minimized when we work with data sets larger than 20,000 galaxies for our mock catalogs, and as our real sample is approximately 6 times larger than that, we are confident that the scatter introduced by our methodology due to this effect is minor.

As a result of these tests, we can estimate the correction factor in the slope needed to make our mock catalog output the same metallicity gradient that we input in each indicator. For our presented results below, we will apply this small correction factor, which should account for some of these effects in the real sample.

#### 4. DATA ANALYSIS AND PROCEDURES

The SDSS Main sample of galaxies does not have many spectra of multiple parts of individual galaxies to study how the metallicity varies as a function of radius in a single object. Instead, this sample was entirely observed with single, central fibers with 3 arcsec diameters. This constant angular aperture means that observing a galaxy at a low redshift will measure the metallicity in a smaller physical aperture around the center of the galaxy than a galaxy observed at higher redshift. This approach follows that of Yan & Blanton (2012), who measured emission lines. Here, we are attempting to localize the absorption lines by stacking galaxies and computing the values in question in annuli of the galaxies.

Each stellar mass bin is handled separately. Within each stellar mass bin, the objects are divided up into redshift bins with the goal of having the maximal number of bins without having any span too large a redshift range or contain too few objects for statistical power. We need to balance the concern of flattening the true gradient by having too few bins (see discussion in Yuan et al. 2013) with the concern that too many bins will cause differentials between bins to be too small to be observed with our uncertainty being on the same order of magnitude as the actual changes. We tested many binning choices and

find that changes to the binning choices have minimal impact in the determination of the gradients, indicating that our results are relatively robust.

Once the stellar mass bins are subdivided into redshift bins, we compute the average value for the line and continuum luminosity of each metallicity indicator measured above for all the galaxies falling into that bin. For details of this sample’s binning, see Table 2.

We then can compute the Lick index for an annulus by calculating

$$\frac{\text{line luminosity}_{z_{\text{bin}1}} - \text{line luminosity}_{z_{\text{bin}2}}}{\text{continuum luminosity}_{z_{\text{bin}1}} - \text{continuum luminosity}_{z_{\text{bin}2}}} \quad (1)$$

for adjacent redshift bins “zbin 1” and “zbin 2.” Knowing the redshift of each object in a redshift bin and the SDSS aperture size (3 arcseconds diameter), we can then compute the average redshift of each galaxy in a bin and then convert that to a physical radius assuming standard cosmology ( $H_0 = 70 \text{ km s}^{-1} \text{ Mpc}^{-1}$ ,  $\Omega_M = 0.3$ ,  $\Omega_\Lambda = 0.7$ ). A radius is then assigned to each annulus by taking the midpoint of the two redshift bins’ physical radii that the annulus is computed from. Thus, we are left with the pairs of points (Lick index, physical radius) for each stellar mass bin, which are plotted in Figure 3 to measure a gradient. The one exception to this is the innermost point — this one is not an annulus but rather just the innermost redshift bin, and it is assigned a radius of half its maximum extent. One important detail that results from treating the innermost bin this way and binning in equal-redshift spacings is that the innermost redshift bin in each mass bin has a very large amount of impact on the gradient calculations — it not only is used twice (once in the difference between bins 1 and 2 and once by itself as the innermost point), but it covers the largest range of radius and has the smallest number of objects of all the redshift bins in that stellar mass bin. Finally, because our annuli are no longer fully independent of each other, there should be nonzero off-diagonal values in the covariance matrix. We neglect these terms and only consider the diagonal variance in plotting error bars for each point and in fitting for gradients.

This analysis is repeated identically, but replacing stellar mass with velocity dispersion in the initial step. We perform this step mainly for confirmation that our derived masses are accurate, but also so that we can more directly compare the results we find to papers that only report trends with velocity dispersion. Below we will present the results for both binning schemes, but as will be seen there are only a small number of differences.

In addition, we also calculate an average galaxy radius for each stellar mass bin using the average elliptical mass-radius relation discussed in several papers (Chiosi et al. 2012; Shen et al. 2003, among others). For high-mass ellipticals such as our sample here, the relation is approximately  $\log R_{1/2} = 0.54 \log M/M_* - 5.25$ . For the stellar mass value, we use the average stellar mass in each stellar mass bin. As mentioned in those papers, this half-mass radius is not strictly identical to the half-light, or effective radius  $R_e$ , but is usually quite close. In this paper we will use  $R_{1/2}$  as a proxy for  $R_e$  in comparison to other works and refer to it as  $R_e$  only from now on. This will allow for better comparison to theoretical works later in

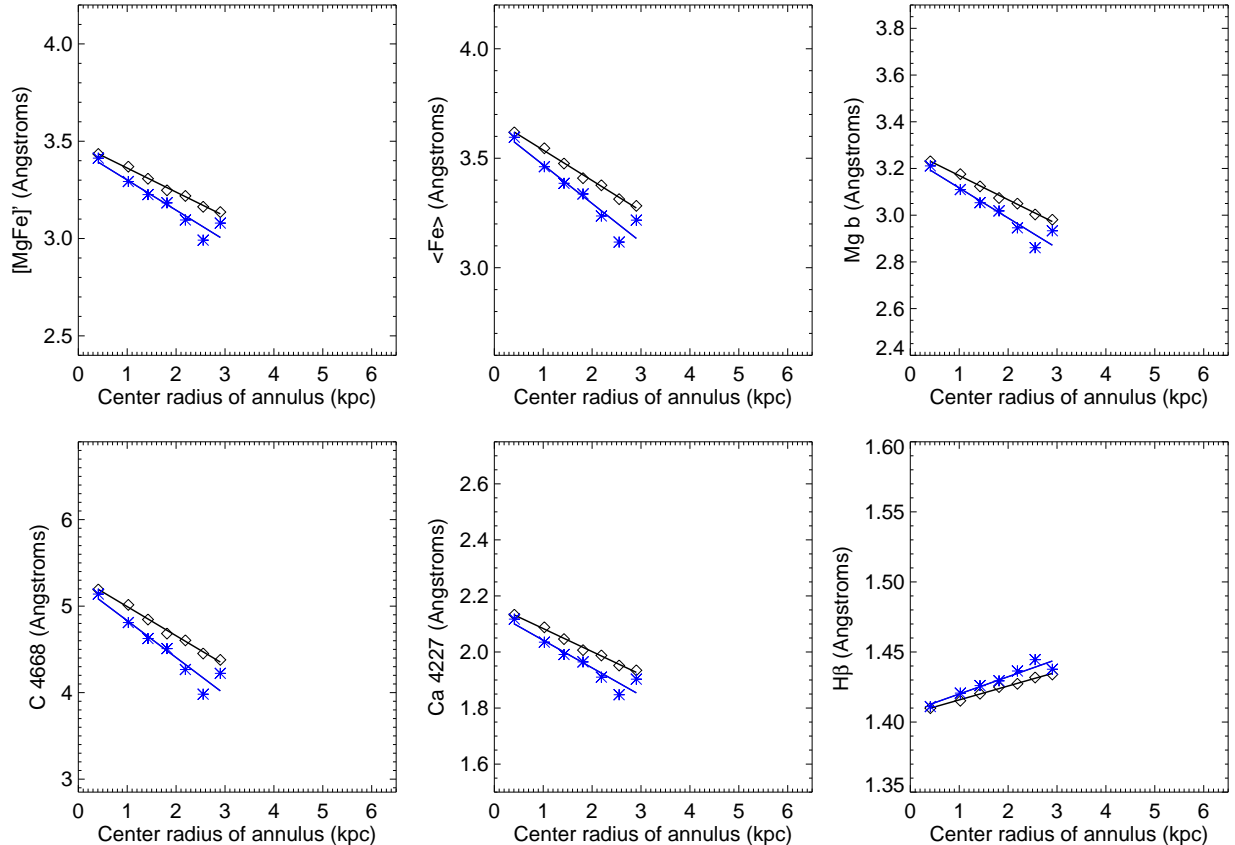


FIG. 2.— Differences between the gradient input to galaxies and the gradient we measure using our annulus method for each indicator. Only one mass bin ( $10.3 < \log(M) < 10.7$ ) is shown for simplicity, but all mass bins were very similar. The input data is shown with black diamonds, and the output measured is shown with blue stars. There is a consistent steepening of the true gradient, as well as a slight constant offset, which we will take into account with a correction factor in our analysis and future plots.

this paper.

With the values computed for the various metallicity indicators in each annulus, we chose to use `EZ_Ages` (Graves & Schiavon 2008) to compute the actual metallicities as well as several other parameters. `EZ_Ages` uses iterative fitting of the stellar population models described in Schiavon (2007) to determine the best-fit metallicity and age from the Lick indices we have measured. We applied `EZ_Ages` to the stacked annuli, not the individual objects. We use solar isochrones and a Salpeter initial mass function with exponent 1.35 as inputs for all galaxies. Changing to  $\alpha$ -enhanced isochrones was tested with minimal impact on the overall results, although a small number of points no longer fit on the age-metallicity grid. The results of the `EZ_Ages` fitting is shown in Figure 4. With metallicities computed, we perform linear regression to compute the gradient for each stellar mass and velocity dispersion bin separately.

One caveat of the use of `EZ_Ages` is that it uses SSP models. As we are averaging over a range of galaxy types and potential evolution paths, the already-approximate SSP approach will have more issues. We thus suggest that care be taken in interpreting the age and metallicity results too strongly.

## 5. RESULTS

Our results are shown in Figures 3–10 below. The first four (Figures 3, 4, 5, and 6) show the results as a function of mass. Figure 3 displays the Lick indices as a function

of physical annulus radius. Figure 4 shows the resulting `EZ_Ages` model parameters as a function of physical radius. Figures 5 and 6 show the same data, but versus  $R/R_e$ , the radius scaled to the galaxy effective radius. The second four (Figures 7–10) show the same results as a function of velocity dispersion.

The lines plotted in all eight are the linear fitting results shown in Table 3 and Table 4 (for stellar mass binning) and Table 5 and Table 6 (for velocity dispersion binning) where the exact values are listed for more precise comparisons. The units are dex  $\text{kpc}^{-1}$  in radius. In addition, we list the line intercept at  $R = 2.5$  kpc and  $R/R_e = 0.5$ , effectively the mean aperture-corrected Lick indices and parameters of early-type SDSS galaxies as a function of mass and velocity dispersion.

Finally, we calculate gradients versus  $\log r$  for  $[\text{Fe}/\text{H}]$ ,  $[\text{Mg}/\text{Fe}]$ , and  $[\text{C}/\text{Fe}]$  for each stellar mass and velocity dispersion bin. These logarithmic gradients are shown in Figures 11 and 12. The values are given in Tables 7 and 8. We find in general very little dependence of the gradients on either mass or velocity dispersion. The only exceptions are a very small trend towards flattening gradients in  $[\text{Fe}/\text{H}]$  as a function of velocity dispersion or mass, with the exception of the lowest velocity dispersion or mass bin gradient of  $[\text{Fe}/\text{H}]$  which is much steeper than the others.

Note that in the above results we found a systematic mis-measurement for one annulus of the  $\text{H}\beta$  line in the

TABLE 2  
BINNING OF GALAXIES IN THIS PAPER

$\log(M)$ Range	Objects	$z$ Min	$z$ Max
$10.0 < \log(M) < 10.3$	754	0.0200	0.0317
$10.0 < \log(M) < 10.3$	1762	0.0317	0.0434
$10.0 < \log(M) < 10.3$	2695	0.0434	0.0550
$10.0 < \log(M) < 10.3$	3835	0.0550	0.0667
$10.0 < \log(M) < 10.3$	6265	0.0667	0.0783
$10.0 < \log(M) < 10.3$	8135	0.0783	0.0900
$10.3 < \log(M) < 10.7$	1273	0.0206	0.0348
$10.3 < \log(M) < 10.7$	2798	0.0348	0.0490
$10.3 < \log(M) < 10.7$	4509	0.0490	0.0632
$10.3 < \log(M) < 10.7$	8548	0.0632	0.0774
$10.3 < \log(M) < 10.7$	11602	0.0774	0.0916
$10.3 < \log(M) < 10.7$	11929	0.0916	0.1058
$10.3 < \log(M) < 10.7$	16872	0.1058	0.1200
$10.7 < \log(M) < 11.0$	830	0.0300	0.0514
$10.7 < \log(M) < 11.0$	2268	0.0514	0.0729
$10.7 < \log(M) < 11.0$	4442	0.0729	0.0943
$10.7 < \log(M) < 11.0$	6107	0.0943	0.1157
$10.7 < \log(M) < 11.0$	9964	0.1157	0.1371
$10.7 < \log(M) < 11.0$	12070	0.1371	0.1586
$10.7 < \log(M) < 11.0$	15466	0.1586	0.1800
$11.0 < \log(M) < 11.5$	691	0.0700	0.0983
$11.0 < \log(M) < 11.5$	1374	0.0983	0.1267
$11.0 < \log(M) < 11.5$	2594	0.1267	0.1550
$11.0 < \log(M) < 11.5$	4092	0.1550	0.1833
$11.0 < \log(M) < 11.5$	5628	0.1833	0.2117
$11.0 < \log(M) < 11.5$	7346	0.2117	0.2400

NOTE. — Details of how galaxies are binned by stellar mass in this paper. A bin is first divided on the basis of the stellar mass of the galaxies (units are solar masses). Following that, the galaxies are divided into bins of equal size in redshift. All the limits are set such that the lower limit is inclusive and the upper is exclusive to avoid overlap.

$10.7 < \log M < 11.0$  mass bin, due to part of the redshift range it covers. The  $H\beta$  line for one bin is redshifted on top of the OI 5577 Å sky line; errors in the sky subtraction at that location lead to an abnormally low flux measured in the line. This leads to  $H\beta$  absorption that appears too large, and an age that is too young, as well as a slight increase in  $[\text{Fe}/\text{H}]$  and  $[\text{Mg}/\text{Fe}]$  for that one point. We retain this data point on all plots, but do not use it in the fits; it is tinted a slightly lighter red in color to indicate the presence of bad data. This issue is not as clearly present in the velocity dispersion binning, likely due to its wider redshift coverage per bin, which dilutes the effect of the error; no masking is used in this case.

There are a wide range of important conclusions to draw from these data. Before moving to discuss them in the context of previous observations and theory, it’s worth simply listing some of the notable facts.

1. All the metal-related Lick indices show a significantly negative gradient when plotted both versus physical radius and  $R/R_e$ .
2. Gradients for stellar population parameters  $[\text{Fe}/\text{H}]$  and  $[\text{C}/\text{Fe}]$  are generally declining, while the gradient for  $[\text{Mg}/\text{Fe}]$  is generally flat.
3. The stellar population ages have very large scatter, with ages ranging from 3 to 12 billion years.
4. There is a slight increase in the central value of  $[\text{C}/\text{Fe}]$  with mass, while the central  $[\text{Fe}/\text{H}]$  and

$[\text{Mg}/\text{Fe}]$  values are nearly constant (where “central” corresponds to the inner 0.5 kpc).

5. The logarithmic gradients have little detectable dependence on mass or velocity dispersion, with the greatest dependence being a slight flattening of the  $[\text{Fe}/\text{H}]$  gradient as those parameters increase.
6. Most of the dependence of the gradient with physical radius on mass is accounted for by the change in  $R_e$  with mass.
7. There are no dramatic differences between the results from the stellar mass binning and the velocity dispersion binning.

We can determine metallicities rather well, but due to the uncertainty in our  $H\beta$  measurements and corrections, our age determinations have a large amount of scatter. Some of the  $H\beta$  uncertainty is driven by the inherent scatter in the [OIII] correction to  $H\beta$  line infill, some results from the extra noise in measuring two lines (instead of one), and some results from the expected slight differences amongst these galaxies that will add some scatter to our points as well. In addition to this, the redshift range that a single data point covers will include some real age differences of the galaxies due to the universe age at that point, which is not accurate if we wish to infer age gradients in an actual galaxy. This effect is at most 2 Gyears across a single bin, though. Due to the lack of trend we find in the age points and the likelihood of these gradients not measuring what we wish to measure, we do not fit to these data points — they are simply shown with error bars at each radius.

We can also see that our stellar mass bins and velocity dispersion bins show similar trends, as we would expect. If we consider the  $R/R_e$  plots (Figures 5, 6, 9, 10; values given in Table 4 and 6), we also find that stellar mass or velocity dispersion only influences the fitted gradients slightly — the  $[\text{Fe}/\text{H}]$  plot shows a steadily increasingly negative central metallicity as stellar mass increases, but the gradient stays mostly constant (contrary to expectations, although similar to recent findings in Pastorello et al. 2014). This trend in central metallicities is loosely reflected in the  $[\text{Mg}/\text{Fe}]'$  and  $\langle \text{Fe} \rangle$  plots as well, as would be expected. Other metals such as  $[\text{C}/\text{Fe}]$  and the indicators C 4668 and Mg b show no clear dependencies on stellar mass in gradient or central values, however.

Below, we will use both the mass and the velocity dispersion results for comparison to prior works, depending on what data the paper in question offers, because our qualitative conclusions are the same regardless.

## 6. COMPARISON TO PREVIOUS OBSERVATIONAL STUDIES

We have three main results: gradients for the EZ\_AGES outputs ( $[\text{Fe}/\text{H}]$ ,  $[\text{C}/\text{Fe}]$ , and age), the trend in their central values with mass, and the trend in their gradients with mass. Each of these have been studied in other papers and we compare with those results here.

Some of the papers we will examine do not use the same stellar population models — they instead use the slightly different models from Thomas et al. (2003) (TMB). These models differ slightly in the outputs they

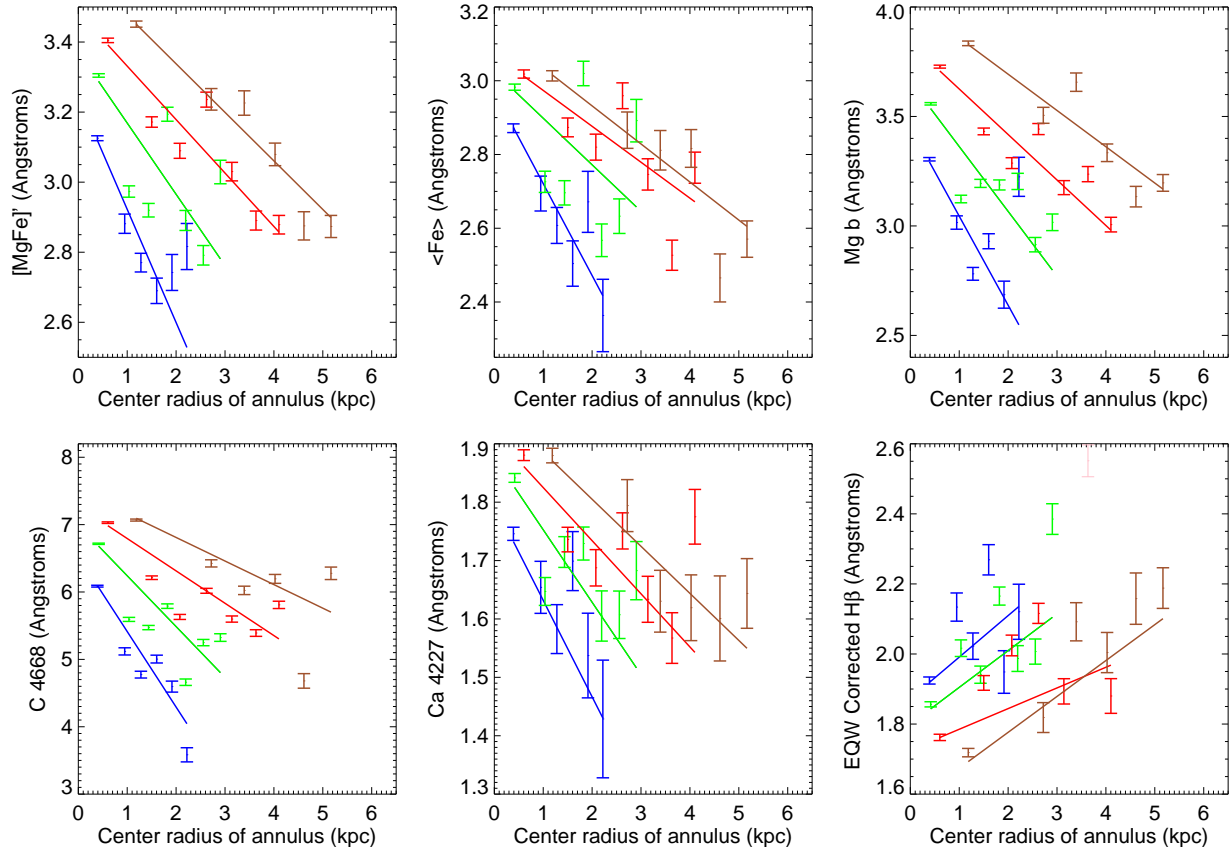


FIG. 3.— The gradients found for each metallicity indicator. Each stellar mass bin is represented with a different color:  $10.0 < \log M < 10.3$  is blue,  $10.3 < \log M < 10.7$  is green,  $10.7 < \log M < 11.0$  is red, and  $11.0 < \log M < 11.5$  is brown

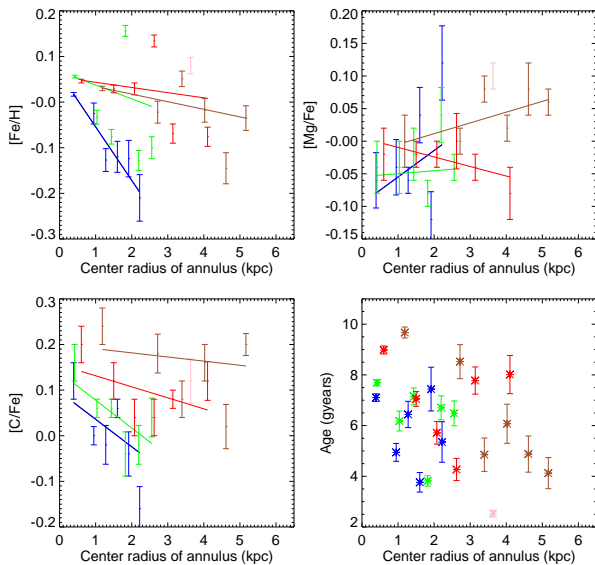


FIG. 4.— The gradients found for the metallicity, age, and several  $[\alpha/\text{Fe}]$  ratios computed using EZ\_Ages. Colors are the same as Figure 3. Binning is done based on stellar mass.

produce, with the TMB models giving  $[\text{Z}/\text{H}]$  and  $[\alpha/\text{Fe}]$  instead of the EZ\_Ages output of  $[\text{Fe}/\text{H}]$ ,  $[\text{Mg}/\text{Fe}]$ , and  $[\text{C}/\text{Fe}]$ . Thomas et al. (2003) proposes a conversion between the two measures of  $[\text{Fe}/\text{H}] = [\text{Z}/\text{H}] - 0.94[\alpha/\text{Fe}]$ ,

which we will use to compare our observations to those papers that use the TMB models. For the  $\alpha$ -elements, the TMB models assume that all  $\alpha$ -elements track Mg, so we can compare our  $[\text{Mg}/\text{Fe}]$  to the  $[\alpha/\text{Fe}]$  values.  $[\text{C}/\text{Fe}]$  will have no analog in those cases.

### 6.1. Gradients

Two large studies integral field studies of the metallicity gradients in inner regions of galaxies cover well the same radial range we cover: Rawle et al. (2010) and Kuntschner et al. (2010). Both these studies measure  $[\text{Z}/\text{H}]$  values out to  $1R_e$ . Both only calculate a  $[\alpha/\text{Fe}]$  ratio (which tracks Mg) and not a  $[\text{C}/\text{Fe}]$  ratio. When applying the  $[\text{Z}/\text{H}]$  to  $[\alpha/\text{Fe}]$  conversion to match our results, both studies find a slightly negative logarithmic metallicity gradient (however, note that the  $[\text{Fe}/\text{H}]$  gradient in Rawle et al. (2010) is consistent with zero), matching our observations — Rawle et al. (2010) finds an average gradient of  $-0.05 \pm 0.05 \text{ dex}^{-1}$  and Kuntschner et al. (2010) finds an average gradient of  $-0.25 \pm 0.11 \text{ dex}^{-1}$ , with values ranging from  $-0.1$  to  $-0.5$  much like our results. Also in agreement with our observations, Kuntschner et al. (2010) report an  $[\alpha/\text{Fe}]$  gradient consistent with zero. Rawle et al. (2010) finds a very slightly negative  $[\alpha/\text{Fe}]$  gradient of  $-0.06 \pm 0.03 \text{ dex}^{-1}$ , which indicates a slight trend unlike our data, but isn't outside of our error bar range.

Mehlert et al. (2003) study the metallicity gradients of early-type galaxies in the Coma Cluster out to about  $R_e$ , also similar to our measurements, using the data

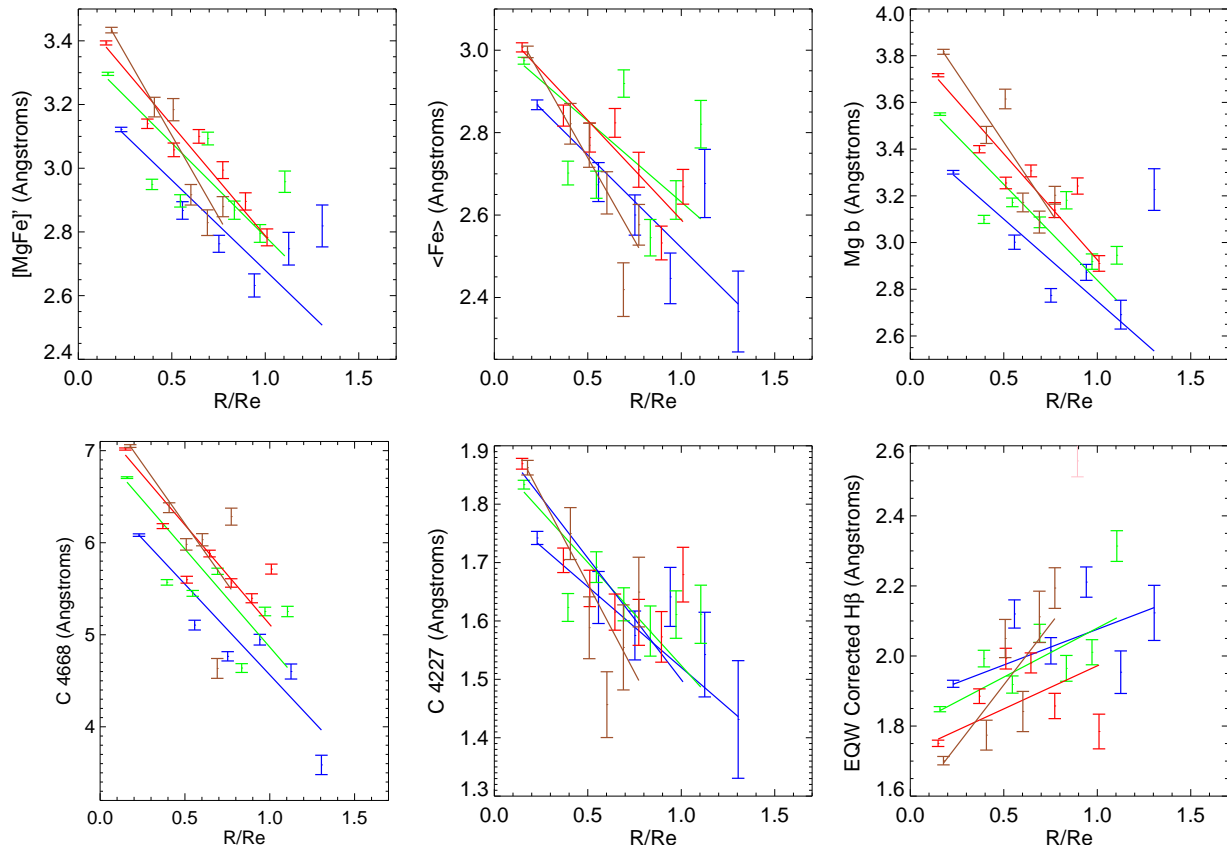


FIG. 5.— Similar to Figure 3, but with all radii scaled to the effective radius. Colors are the same as Figure 3. Binning is done based on stellar mass.

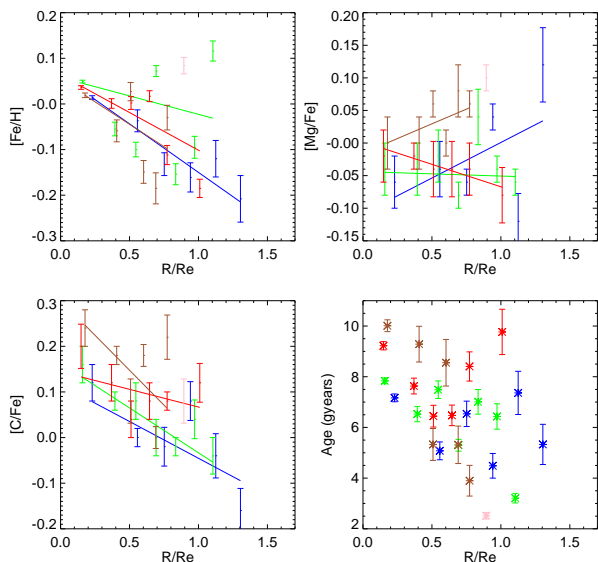


FIG. 6.— Similar to Figure 4, but with all radii scaled to the effective radius. Colors are the same as Figure 3. Binning is done based on stellar mass.

from Mehlert et al. (2000). Rather than using EZ\_Ages to model the metallicity and age, they use the models of Thomas et al. (2003), with the differences discussed above. The results in Mehlert et al. (2003) show declining  $[Z/H]$  and constant age and  $[\alpha/Fe]$  gradient. We can

calculate similar logarithmic index gradients (per Equation 5 in Mehlert et al. 2003, given in Table 7) to compare the values of the metallicity indicators in our stacked annuli to their results. Their  $[Z/H]$  gradient matches our  $[Fe/H]$  gradient well, with a gradient of around  $-0.1$  to  $-0.2$ .

Spolaor et al. (2010) cover a slightly larger range of radii, out to between 1 and  $3 R_e$ . They analyzed 14 low-mass ellipticals in the Fornax and Virgo clusters and compared them to several higher mass ellipticals from previous studies. They interpret the stellar populations using the models of Thomas et al. (2003). They find a declining  $[Z/H]$  ( $-0.22 \pm 0.14$  averaged across all mass bins) and roughly constant  $[\alpha/Fe]$  gradient, in agreement with our results.

Greene et al. (2013) study gradients in 33 nearby galaxies, also out to a much larger radius of the galaxies than we do, about 14 kpc. They measure similar metallicity indicators to our survey, also using EZ\_Ages to convert the data into physical parameters. They find a  $[Fe/H]$  gradient of around  $-0.3$  to  $-0.5$  dex  $kpc^{-1}$ , significantly steeper than ours (Note that here they report gradients versus radius rather than versus logarithmic radius). This discrepancy may indicate that the metallicity gradients steepen in the outer parts of galaxies. Their findings for  $[Mg/Fe]$  and  $[C/Fe]$  are similar to ours, with a constant  $[Mg/Fe]$  gradient in both velocity dispersion bins like all four of ours, and a  $[C/Fe]$  gradient of around  $-0.1$  to  $-0.2$  dex  $kpc^{-1}$  as our data shows as well.

Because the  $[\alpha/Fe]$  gradients are relatively flat in all



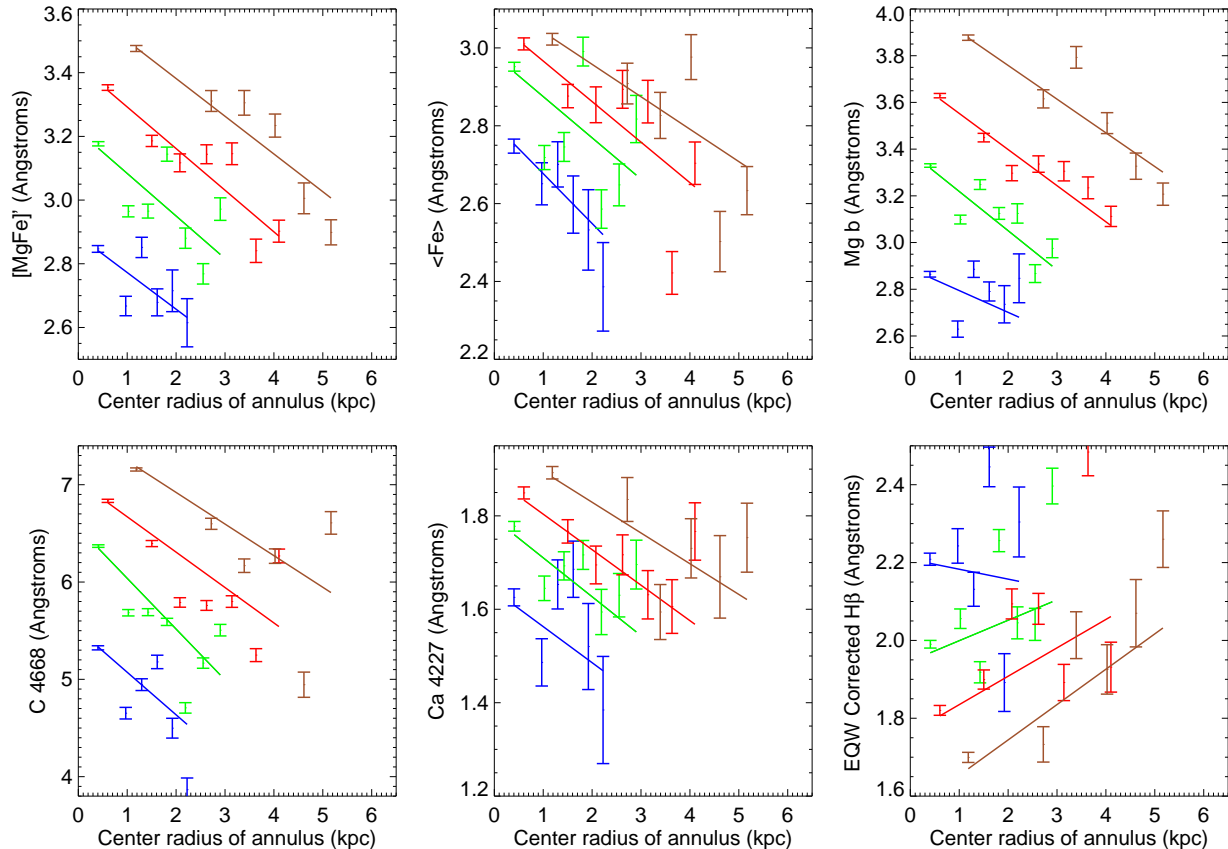


FIG. 7.— The gradients found for each metallicity indicator, but with the initial binning done by velocity dispersion and not stellar mass. Each velocity dispersion bin is a different color: 30 km s<sup>-1</sup> to 125 km s<sup>-1</sup> blue, 125 km s<sup>-1</sup> to 185 km s<sup>-1</sup> green, 185 km s<sup>-1</sup> to 230 km s<sup>-1</sup> red, 230 km s<sup>-1</sup> to 325 km s<sup>-1</sup> brown.

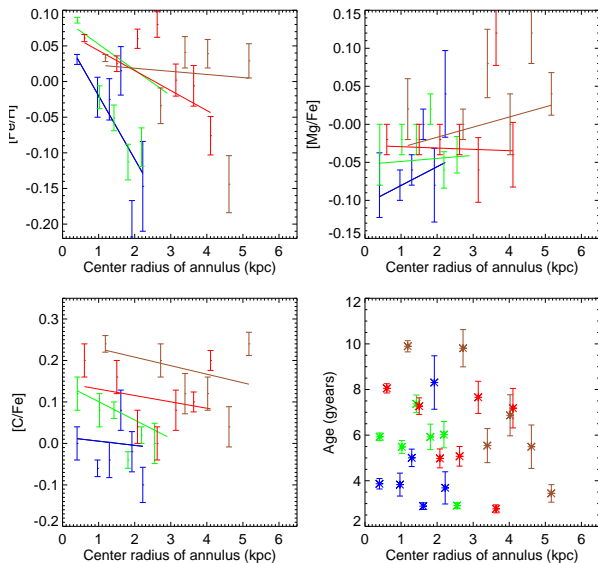


FIG. 8.— The gradients found for the metallicity, age, and several  $[\alpha/\text{Fe}]$  ratios computed using EZ\_Ages. Colors are the same as Figure 7. and binning is done on the basis of velocity dispersion.

cases aside from that of Rawle et al. (2010), it is reasonable that our  $[\text{Fe}/\text{H}]$  results and the  $[\text{Z}/\text{H}]$  results from these studies are in agreement.

## 6.2. Trend in central values with mass

We next turn to trends with mass in the stellar population parameters at the centers of galaxies. Our centermost bins are  $R \sim 0.2R_e$  or  $\sim 0.5$  kpc. We find only weak (at best) trends with mass. Central  $[\text{Fe}/\text{H}]$  shows a dependence that is not monotonic and is  $< 0.1$  dex across our whole sample. Central  $[\text{Mg}/\text{Fe}]$  shows an small increase with velocity dispersion that is  $\sim 0.1$  dex across our whole range of masses or velocity dispersion, but the same trend does not exist for mass binning

Kuntschner et al. (2010) reports their central values at  $R_e/8$ , slightly more internal than ours but comparable. They too find no monotonic dependence of the central metallicities on velocity dispersion or mass, although their results have more scatter (ranging from 0.2 to around  $-0.4$ ) after we apply the  $[\text{Z}/\text{H}]$  to  $[\text{Fe}/\text{H}]$  conversion. Again similarly, they find that the central  $[\alpha/\text{Fe}]$  does increase with mass or velocity dispersion, although there is a constant offset of about 0.2 dex higher in their central values than we find, part of which can be explained by the more central location. Their trend is much clearer than ours is as well.

Turning to Rawle et al. (2010), we find central values recorded at  $R_e/3$ , again comparable to our central annulus radius. As with Kuntschner et al. (2010), after converting their reported  $[\text{Z}/\text{H}]$  values to  $[\text{Fe}/\text{H}]$ , there is no clear trend with central velocity dispersion and a larger scatter than we report. Their  $[\alpha/\text{Fe}]$  central trend with central velocity dispersion also matches ours with

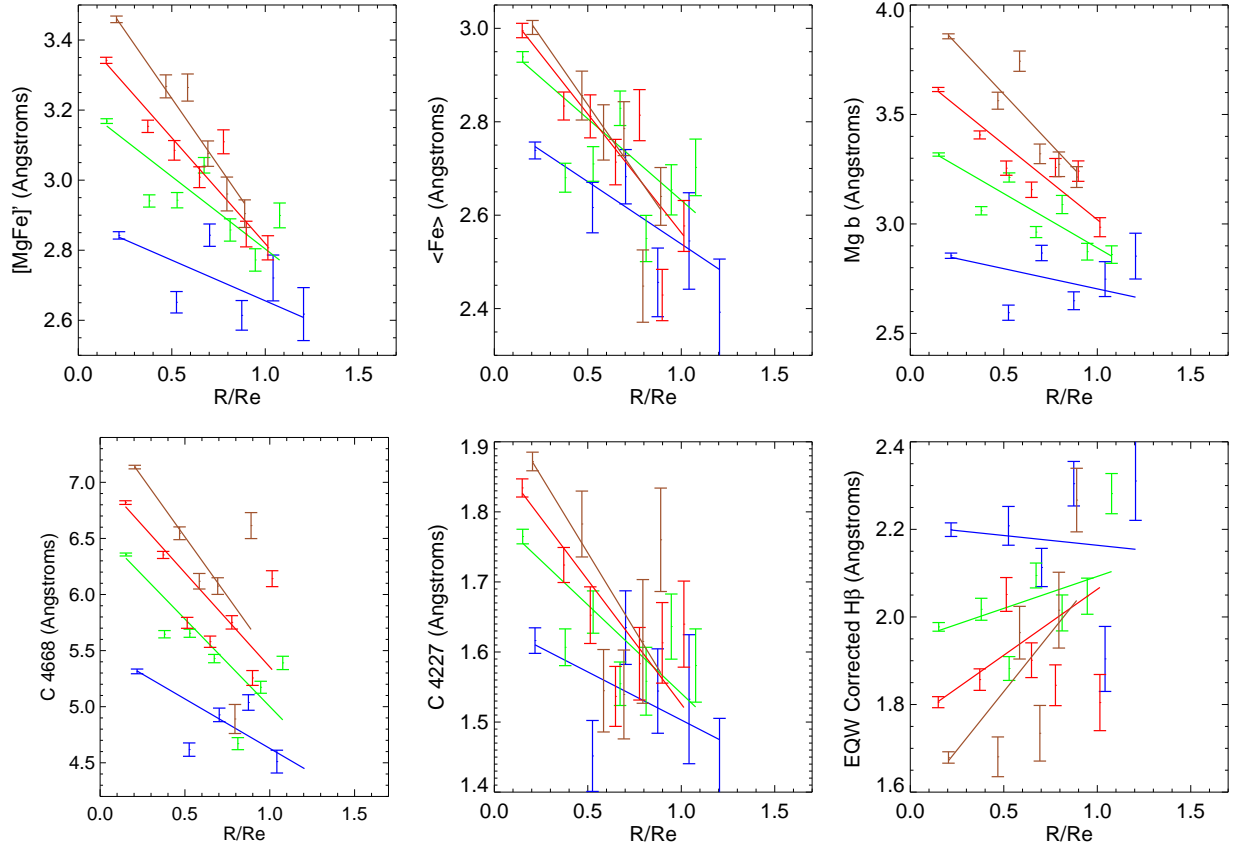


FIG. 9.— Similar to Figure 7, but with all radii scaled to the effective radius. Colors are the same as Figure 7. Binning is done based on velocity dispersion.

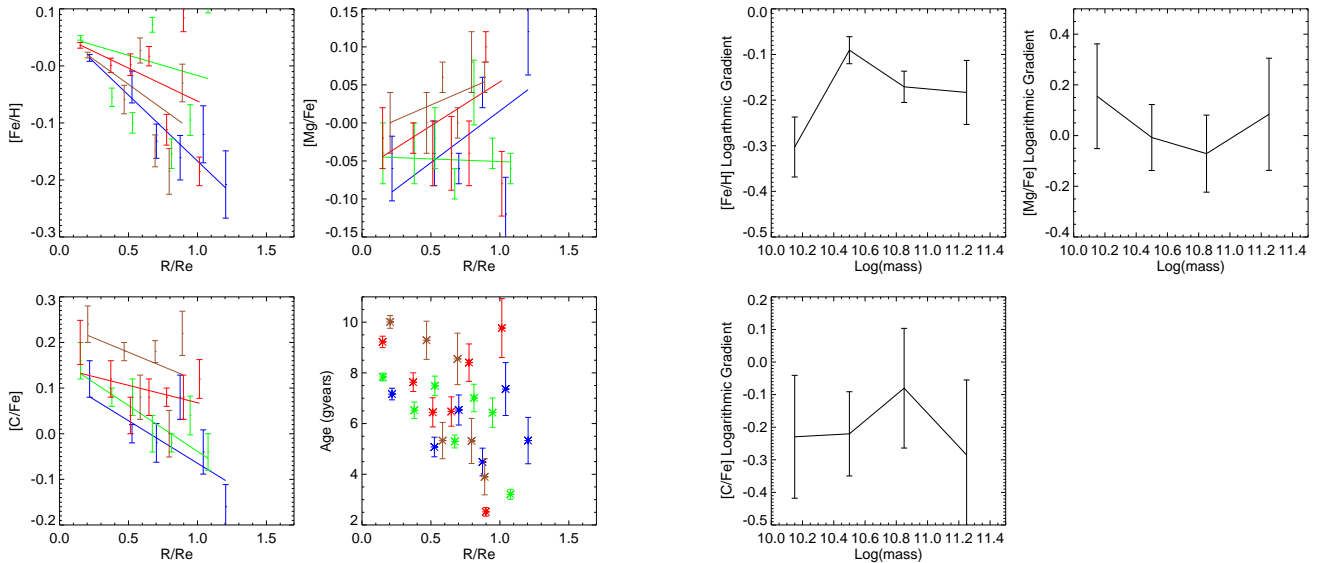


FIG. 10.— Similar to Figure 8, but with all radii scaled to the effective radius. Colors are the same as Figure 7. Binning is done based on velocity dispersion.

an increase as velocity dispersion increases, but as with Kuntschner et al. (2010), they also find systematically higher values for the central  $[\alpha/\text{Fe}]$  than we record and a clearer indication of the trend than we see.

FIG. 11.— The stellar mass dependence of the  $[\text{Fe}/\text{H}]$ ,  $[\text{Mg}/\text{Fe}]$ , and  $[\text{C}/\text{Fe}]$  logarithmic gradients as calculated in Table 7. Broadly speaking we find a constant  $[\text{Fe}/\text{H}]$  (with the exception of the lowest stellar mass bin which shows a much steeper gradient),  $[\text{Mg}/\text{Fe}]$  and  $[\text{C}/\text{Fe}]$  gradient as a function of stellar mass.

Spolaor et al. (2010) detect an increase with mass of central  $[\text{Z}/\text{H}]$  and  $[\alpha/\text{Fe}]$  at radii similar to the smallest radii we probe ( $R_e/8$ ); between 100 and 300  $\text{km s}^{-1}$

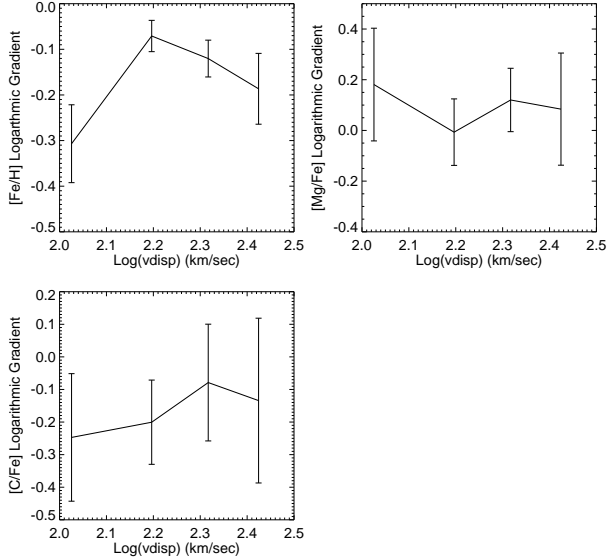


FIG. 12.— The velocity dispersion dependence of the  $[\text{Fe}/\text{H}]$ ,  $[\text{Mg}/\text{Fe}]$ , and  $[\text{C}/\text{Fe}]$  logarithmic gradients as calculated in Table 8. Broadly speaking we find a very slightly flattening  $[\text{Fe}/\text{H}]$  gradient, and a constant  $[\text{Mg}/\text{Fe}]$  and  $[\text{C}/\text{Fe}]$  gradient as a function of velocity dispersion.

they detect an increase in  $[\text{Z}/\text{H}]$  of 0.3 dex and in  $[\alpha/\text{Fe}]$  of 0.2 dex. When applying the conversion from  $[\text{Z}/\text{H}]$  to  $[\text{Fe}/\text{H}]$ , this is close to our results, although a slight central  $[\text{Fe}/\text{H}]$  increase as a function of velocity still remains that we do not detect and the dependence of  $[\alpha/\text{Fe}]$  is stronger than what we find, matching more closely Kuntschner et al. (2010) and Rawle et al. (2010).

Using data with similar radial coverage, Mehlert et al. (2003) found similar dependences. These results indicate stronger mass dependence than we find by about 0.1 dex over this range for  $[\alpha/\text{Fe}]$ . Assuming the conversion about between  $[\text{Z}/\text{H}]$  and  $[\text{Fe}/\text{H}]$  it also implies a stronger mass dependence in  $[\text{Fe}/\text{H}]$  than we find, also by about 0.1 dex.

The galaxies in Greene et al. (2013) also show an increase in central metallicity with mass at a fixed radius, but their centermost bin is around 2–3 kpc. Our galaxies show a similar trend at that physical radius. The trends with mass agree with those in Greene et al. (2013) in the  $[\text{C}/\text{Fe}]$  and  $[\text{Mg}/\text{Fe}]$  ratio, with the former showing slight increase at all our radii with stellar mass, and the latter being roughly constant. This trend with mass persists across all radii in our survey (with the exception of the lowest mass or velocity dispersion bin).

### 6.3. Trend in gradients with mass

Figures 11 and 12 show the logarithmic gradients as a function of stellar mass and velocity dispersion. Our metallicity gradients are close to constant or perhaps slightly steepening within the errors as stellar mass increases with the only exception being the lowest stellar mass and velocity dispersion bins. In the higher mass bins, the  $[\text{Fe}/\text{H}]$  gradient anti-correlates with both the stellar mass and the velocity dispersion; however, both trends are very low significance. For  $[\text{Mg}/\text{Fe}]$  and  $[\text{C}/\text{Fe}]$ , we find no significant trends in the gradients as a function

of mass or velocity dispersion.

Both Rawle et al. (2008) and its followup paper, Rawle et al. (2010), as well as Kuntschner et al. (2010) find a large amount of scatter in gradients. Kuntschner et al. (2010) note a slight trend that is partially reflected in our data. At low masses, Kuntschner et al. (2010) reports an increasingly negative metallicity gradient (up to about  $3.5 \times 10^{10}$  solar masses), followed by a flattening metallicity gradient as mass increases further. We have far fewer points to use to determine trends with mass, but our lowest-mass point is indeed the steepest gradient, with all higher-mass ones showing some evidence of flattening out (see Figures 11 and 12, and Tables 7 and 8). However the granularity of our data prevents us from checking in detail at which mass we find this turnover to be at to further compare to the observations in Kuntschner et al. (2010).

Spolaor et al. (2010) also covers enough of a stellar mass range to check for any mass dependency of these gradients, and does find a slight flattening of the metallicity gradient as stellar mass increases for high-mass ellipticals, although the scatter increases significantly as well. The bins that overlap most completely (covering a range of velocity dispersions  $2.1 < \log \sigma < 2.6$ ) have very similar measured gradients as a function of  $R/R_e$  ( $-0.2$  to  $-0.4$  in Spolaor et al. (2010) and  $-0.15$  to  $-0.25$  in our sample), although the trend is reversed.

The work of Ogando et al. (2006) provides another reference on metallicity gradients for us to compare to. Ogando et al. (2006) measure  $\text{Mg}_2$  and  $\text{H}\beta$  only to supply to the TMB stellar models, with a forced  $[\alpha/\text{Fe}]$  of 0.3, slightly higher than our model fits would predict, but within most of the error bars. With that, they find  $[\text{Fe}/\text{H}]$  logarithmic gradients (converted from the  $[\text{Z}/\text{H}]$  gradients in the paper) ranging from  $-0.1$  to  $-1.2$ , but with the bulk of the galaxies found to have gradients between  $-0.3$  and  $-0.8$ . They record these as functions of galaxy stellar velocity dispersion and mass, and find a slight trend to a steepening  $[\text{Fe}/\text{H}]$  gradient as mass or velocity dispersion increases, matching our 3 highest mass bins; however, the scatter is large. This is in agreement with the results in Kuntschner et al. (2010) and our results, although again, the observed steepening with increased mass is paired with an increase in scatter as well.

Finally, at the larger radii that Greene et al. (2013) measure, they find qualitatively similar trends, with roughly constant gradients in all indicators as a function of mass.

As will be discussed more in Section 7, the scatter observed in the gradients could be due to the wide variety of merger histories available to high-mass ellipticals (Di Matteo et al. 2009), leading to a wide variety of potential final, observed gradients for individual galaxies.

Realistically, the large error bars present in the determination of the metallicity gradients prevent us from concluding anything too firm; we mostly can say that it appears that the gradient very slightly flattens with increasing stellar mass or velocity dispersion, and is close to constant or slightly declining above a certain stellar mass or velocity dispersion cutoff around  $3 \times 10^{10}$  solar masses, which is not in disagreement with any of the studies we found.

### 6.4. General conclusions

There is good agreement with finding a negative  $[\text{Fe}/\text{H}]$  gradient, a constant  $[\text{Mg}/\text{Fe}]$ , and a very slightly negative  $[\text{C}/\text{Fe}]$  gradient, even if the numerical results presented have a fairly large amount of scatter. For trends in central values as mass (or velocity dispersion) increases, we find general agreement with an increasing central  $[\text{Mg}/\text{Fe}]$  (although our dependence is less than other compared studies by about 0.1 dex) and constant central  $[\text{Fe}/\text{H}]$ , and increasing central  $[\text{C}/\text{Fe}]$  (where central in this data set means within  $\sim 0.5$  kpc).

Finally, we find that in general we agree with the most of the reported trends in gradients of  $[\text{Fe}/\text{H}]$  with mass as well — with the most negative gradient in the lowest mass objects, and then a flatter although still negative gradient for higher mass galaxies, with the gradient leveling out to be roughly constant with mass or perhaps very slightly steepening.  $[\text{Mg}/\text{Fe}]$  shows agreement here as well, with no real trends reported with mass in the gradients.

Because it is a statistical average, our data set is not sensitive to the increase in scatter with mass found by Kuntschner et al. (2010) and others in the  $[\text{Fe}/\text{H}]$  gradient.

## 7. COMPARISON TO THEORY

According to a number of theoretical investigations, mergers tend to flatten gradients and monolithic collapse models tend to steepen them (Pipino et al. 2010; Di Matteo et al. 2009). Because the detailed history of each galaxy’s growth involves some features of both monolithic collapse and hierarchical merging models, the predicted results lie along a continuum of flat to steep gradients, with substantial scatter amongst the results due to differing degrees of these two effects for each individual galaxy (Pipino et al. 2010). Thus we do not expect perfect agreement with any individual models but rather that our data lie somewhere in between results reported by merger-focused simulations and monolithic collapse-focused simulations.

When comparing our gradient values to those in Hopkins et al. (2009), who simulated merger models, we find general agreement. Most of their metallicity gradients are between  $-0.1$  and  $-0.6$ , while our results (shown in Table 7) are around  $-0.1$  to  $-0.4$  dex. Similar conclusions are drawn by Kobayashi (2003) who finds gradients in the range of  $-0.2$  to  $-0.8$ . Kobayashi (2003) simulates both merging and monolithically collapsing galaxies, and it is important to note that within the spread of the results, our data agrees with both sets. Because there is likely to be natural variation among galaxies in our sample, we do not rule out that some galaxies have the steep gradients predicted by models. Di Matteo et al. (2009) handles mergers in more detail than most simulations, measuring gradients that result from various mass ratios and various initial metallicity gradients of merging galaxies. The results again show metallicity gradients of about  $-0.1$  to  $-0.4$ , but are dependent on the type of mergers that have occurred to form the final galaxies as expected. For reasonable initial metallicity gradients and merger histories, our results appear in agreement with the simulations of Di Matteo et al. (2009).

Another interesting property to investigate is the stellar mass trend. Our results (see Figure 11) suggest that all three gradients are roughly constant with stellar

mass, with perhaps a slightly flattening  $[\text{Fe}/\text{H}]$  depending on how much the lowest stellar mass bin is to be believed. Simulations give varied results depending on the merger history of the galaxies, with Di Matteo et al. (2009) noting processes that can give rise to both flatter and steeper gradients depending on the stellar masses of merging galaxies and their initial gradients, and thus proposing that little trend should exist overall but scatter should increase. Other models predict no clear trend and increasing scatter as well (see Pipino et al. 2010; Kobayashi 2003). Some models do predict a correlation (Kawata & Gibson 2003), but only take into account monolithic collapse and not the interplay of mergers as well. In general, though, the conclusions are broadly suggestive that metallicity gradients should slightly steepen with increasing stellar mass, albeit with increased scatter as well (Ogando et al. 2005) due to higher stellar mass galaxies being allowed a larger variety of possible evolution paths that will change how their gradients develop. We find no clear trend in  $[\text{Fe}/\text{H}]$  gradient with stellar mass or velocity dispersion, with only a weakly detected flattening. The error bars in our results are largely driven by statistical considerations based on the number of objects in each stellar mass bin, so we are unable to detect any potential intrinsic scatter in the data that may exist due to our method.

The potential for many types of mergers and the differing gradients that result from the different stellar mass ratios and initial metallicity gradients of the progenitors as discussed in detail in Di Matteo et al. (2009) make it difficult to conclude definitively if our observations agree with theory as simply adjusting the progenitor properties within reasonable values can change the model predictions dramatically. To make a more detailed comparison of our results to theory would require modeling expected merger rates and stellar mass ratios. However, for now, we can conclude that our results do not indicate any clear disagreements — the gradients we find are within the ranges predicted by models that incorporate both monolithic collapse and mergers of many types into the evolution of elliptical galaxies, and our gradients follow a generally observed trend with stellar mass.

## 8. CONCLUSIONS

The approach used here has drawbacks and challenges but also significant advantages relative to previous studies. We can determine only mean metallicity and abundance gradients, with little power to constrain how the gradients are distributed about the mean. However, by being able to work with single-spectrum galaxies, we potentially can examine a much larger sample of galaxies than previously possible.

Relative to previous studies, our measured gradients in  $[\text{Fe}/\text{H}]$  are similar but on the whole slightly shallower, while our  $[\text{Mg}/\text{Fe}]$  gradient matches all the compared studies by being flat. In terms of stellar mass dependence, we see a flattening of metallicity gradients as mass increases in line with the compared studies. We find fairly similar central values for  $[\alpha/\text{Fe}]$  (although slightly smaller), and also observe an increase in central  $[\alpha/\text{Fe}]$  with stellar mass as the other studies do. Our metallicity also matches previous studies both in values and trends with mass.

In sum, we find that using this new technique to

find the metallicity inside an annulus of averaged galaxies roughly agrees with both observations of individual galaxies and simulated predictions of galaxies that have formed from mergers and/or monolithic collapse, a conclusion which is supported by our analysis of mock data to ensure this method is valid.

This technique may be of further use. With this same data set, one could extend the analysis to include the broader wavelength range accessible to the SDSS spectrograph than to most integral field observations. In addition, this technique could be used for some higher redshift surveys to measure a similar mean gradient for galaxies at higher redshift, for example in the AGN and Galaxy Evolution Survey (AGES), GAMA, or the planned DESI Bright Galaxy Survey.

We thank the referee for many helpful comments, especially in directing us to consider simulations to confirm our method's validity.

Funding for the SDSS and SDSS-II has been provided by the Alfred P. Sloan Foundation, the Participating Institutions, the National Science Foundation, the U.S. Department of Energy, the National Aeronautics and Space Administration, the Japanese Monbukagakusho, the Max Planck Society, and the Higher Education Funding Council for England. The SDSS Web Site is <http://www.sdss.org/>.

The SDSS is managed by the Astrophysical Research Consortium for the Participating Institutions. The Participating Institutions are the American Museum of Natural History, Astrophysical Institute Potsdam, University of Basel, University of Cambridge, Case Western Reserve University, University of Chicago, Drexel University, Fermilab, the Institute for Advanced Study, the Japan Participation Group, Johns Hopkins University, the Joint Institute for Nuclear Astrophysics, the Kavli Institute for Particle Astrophysics and Cosmology, the Korean Scientist Group, the Chinese Academy of Sciences (LAMOST), Los Alamos National Laboratory, the Max-Planck-Institute for Astronomy (MPIA), the Max-Planck-Institute for Astrophysics (MPA), New Mexico State University, Ohio State University, University of Pittsburgh, University of Portsmouth, Princeton University, the United States Naval Observatory, and the University of Washington.

TABLE 3  
GRADIENTS IN METALLICITY INDICATORS VERSUS PHYSICAL RADIUS

Measure	log $M$ Range	Gradient	Uncertainty in Gradient	Value at 2.5 kpc
$[MgFe]'$	$10.0 < \log(M) < 10.3$	-0.3229	0.0165	2.4379
$[MgFe]'$	$10.3 < \log(M) < 10.7$	-0.2035	0.0071	2.8636
$[MgFe]'$	$10.7 < \log(M) < 11.0$	-0.1526	0.0050	3.1023
$[MgFe]'$	$11.0 < \log(M) < 11.5$	-0.1385	0.0059	3.2685
$\langle Fe \rangle$	$10.0 < \log(M) < 10.3$	-0.2493	0.0274	2.3472
$\langle Fe \rangle$	$10.3 < \log(M) < 10.7$	-0.1262	0.0119	2.7090
$\langle Fe \rangle$	$10.7 < \log(M) < 11.0$	-0.0974	0.0081	2.8277
$\langle Fe \rangle$	$11.0 < \log(M) < 11.5$	-0.1032	0.0093	2.8801
Mg b	$10.0 < \log(M) < 10.3$	-0.4068	0.0182	2.4345
Mg b	$10.3 < \log(M) < 10.7$	-0.2961	0.0081	2.9186
Mg b	$10.7 < \log(M) < 11.0$	-0.2078	0.0059	3.3138
Mg b	$11.0 < \log(M) < 11.5$	-0.1658	0.0071	3.6103
C 4668	$10.0 < \log(M) < 10.3$	-1.1205	0.0282	3.7319
C 4668	$10.3 < \log(M) < 10.7$	-0.7542	0.0123	5.1096
C 4668	$10.7 < \log(M) < 11.0$	-0.4804	0.0092	6.0734
C 4668	$11.0 < \log(M) < 11.5$	-0.3499	0.0133	6.6346
Ca 4227	$10.0 < \log(M) < 10.3$	-0.1652	0.0247	1.3840
Ca 4227	$10.3 < \log(M) < 10.7$	-0.1241	0.0104	1.5666
Ca 4227	$10.7 < \log(M) < 11.0$	-0.0910	0.0077	1.6885
Ca 4227	$11.0 < \log(M) < 11.5$	-0.0806	0.0100	1.7647
Corrected H $\beta$	$10.0 < \log(M) < 10.3$	0.1185	0.0210	2.1687
Corrected H $\beta$	$10.3 < \log(M) < 10.7$	0.1049	0.0095	2.0620
Corrected H $\beta$	$10.7 < \log(M) < 11.0$	0.0590	0.0084	1.8736
Corrected H $\beta$	$11.0 < \log(M) < 11.5$	0.1025	0.0099	1.8275
$[Fe/H]$	$10.0 < \log(M) < 10.3$	-0.1171	0.0135	-0.2301
$[Fe/H]$	$10.3 < \log(M) < 10.7$	-0.0301	0.0058	-0.0079
$[Fe/H]$	$10.7 < \log(M) < 11.0$	-0.0114	0.0039	0.0264
$[Fe/H]$	$11.0 < \log(M) < 11.5$	-0.0166	0.0043	0.0092
$[Mg/Fe]$	$10.0 < \log(M) < 10.3$	0.0407	0.0309	0.0061
$[Mg/Fe]$	$10.3 < \log(M) < 10.7$	0.0046	0.0179	-0.0430
$[Mg/Fe]$	$10.7 < \log(M) < 11.0$	-0.0146	0.0117	-0.0315
$[Mg/Fe]$	$11.0 < \log(M) < 11.5$	0.0165	0.0089	0.0198
$[C/Fe]$	$10.0 < \log(M) < 10.3$	-0.0602	0.0252	-0.0543
$[C/Fe]$	$10.3 < \log(M) < 10.7$	-0.0611	0.0218	-0.0136
$[C/Fe]$	$10.7 < \log(M) < 11.0$	-0.0242	0.0136	0.0951
$[C/Fe]$	$11.0 < \log(M) < 11.5$	-0.0091	0.0108	0.1771

NOTE. — The calculated gradients for each measured metallicity indicator and the EZ\_Ages results binned by stellar mass. The units are dex kpc<sup>-1</sup>.

TABLE 4  
GRADIENTS IN METALLICITY INDICATORS VERSUS SCALED RADIUS

Measure	log $M$ Range	Gradient	Uncertainty in Gradient	Value at $0.5 R_e$
$[MgFe]'$	$10.0 < \log(M) < 10.3$	-0.5658	0.0281	2.9623
$[MgFe]'$	$10.3 < \log(M) < 10.7$	-0.5865	0.0187	3.0790
$[MgFe]'$	$10.7 < \log(M) < 11.0$	-0.6961	0.0202	3.1358
$[MgFe]'$	$11.0 < \log(M) < 11.5$	-1.0237	0.0394	3.1031
$\langle Fe \rangle$	$10.0 < \log(M) < 10.3$	-0.4494	0.0466	2.7456
$\langle Fe \rangle$	$10.3 < \log(M) < 10.7$	-0.3929	0.0312	2.8281
$\langle Fe \rangle$	$10.7 < \log(M) < 11.0$	-0.4828	0.0327	2.8298
$\langle Fe \rangle$	$11.0 < \log(M) < 11.5$	-0.7990	0.0623	2.7386
Mg b	$10.0 < \log(M) < 10.3$	-0.7023	0.0310	3.1003
Mg b	$10.3 < \log(M) < 10.7$	-0.8199	0.0213	3.2489
Mg b	$10.7 < \log(M) < 11.0$	-0.9070	0.0240	3.3797
Mg b	$11.0 < \log(M) < 11.5$	-1.1906	0.0475	3.4294
C 4668	$10.0 < \log(M) < 10.3$	-1.9689	0.0480	5.5489
C 4668	$10.3 < \log(M) < 10.7$	-2.1291	0.0322	5.9306
C 4668	$10.7 < \log(M) < 11.0$	-2.1628	0.0374	6.1929
C 4668	$11.0 < \log(M) < 11.5$	-2.6084	0.0891	6.2052
Ca 4227	$10.0 < \log(M) < 10.3$	-0.2767	0.0420	1.6587
Ca 4227	$10.3 < \log(M) < 10.7$	-0.3531	0.0274	1.7002
Ca 4227	$10.7 < \log(M) < 11.0$	-0.4164	0.0314	1.7078
Ca 4227	$11.0 < \log(M) < 11.5$	-0.6056	0.0671	1.6634
Corrected $H\beta$	$10.0 < \log(M) < 10.3$	0.2036	0.0358	1.9744
Corrected $H\beta$	$10.3 < \log(M) < 10.7$	0.2800	0.0249	1.9396
Corrected $H\beta$	$10.7 < \log(M) < 11.0$	0.2458	0.0342	1.8490
Corrected $H\beta$	$11.0 < \log(M) < 11.5$	0.6925	0.0663	1.9176
$[Fe/H]$	$10.0 < \log(M) < 10.3$	-0.2127	0.0228	-0.0437
$[Fe/H]$	$10.3 < \log(M) < 10.7$	-0.0808	0.0132	0.0176
$[Fe/H]$	$10.7 < \log(M) < 11.0$	-0.1652	0.0154	-0.0189
$[Fe/H]$	$11.0 < \log(M) < 11.5$	-0.1966	0.0294	-0.0446
$[Mg/Fe]$	$10.0 < \log(M) < 10.3$	0.1090	0.0483	-0.0537
$[Mg/Fe]$	$10.3 < \log(M) < 10.7$	-0.0067	0.0369	-0.0473
$[Mg/Fe]$	$10.7 < \log(M) < 11.0$	-0.0689	0.0558	-0.0326
$[Mg/Fe]$	$11.0 < \log(M) < 11.5$	0.0902	0.0653	0.0295
$[C/Fe]$	$10.0 < \log(M) < 10.3$	-0.1611	0.0469	0.0352
$[C/Fe]$	$10.3 < \log(M) < 10.7$	-0.1965	0.0410	0.0648
$[C/Fe]$	$10.7 < \log(M) < 11.0$	-0.0777	0.0601	0.1057
$[C/Fe]$	$11.0 < \log(M) < 11.5$	-0.3059	0.0717	0.1476

NOTE. — The calculated gradients for each measured metallicity indicator and the EZ-Ages results binned by stellar mass. The units are dex.

TABLE 5  
GRADIENTS IN METALlicity INDICATORS VERSUS PHYSICAL RADIUS

Measure	$\sigma$ Range (km s <sup>-1</sup> )	Gradient	Uncertainty in Gradient	Value at 2.5 kpc
[MgFe]'	30 < $\sigma$ < 125	-0.1152	0.0204	2.5996
[MgFe]'	125 < $\sigma$ < 185	-0.1336	0.0082	2.8832
[MgFe]'	185 < $\sigma$ < 230	-0.1307	0.0066	3.0963
[MgFe]'	230 < $\sigma$ < 325	-0.1185	0.0069	3.3224
< Fe >	30 < $\sigma$ < 125	-0.1281	0.0341	2.4848
< Fe >	125 < $\sigma$ < 185	-0.1060	0.0137	2.7160
< Fe >	185 < $\sigma$ < 230	-0.1042	0.0108	2.8100
< Fe >	230 < $\sigma$ < 325	-0.0833	0.0109	2.9161
Mg b	30 < $\sigma$ < 125	-0.0934	0.0230	2.6544
Mg b	125 < $\sigma$ < 185	-0.1679	0.0094	2.9668
Mg b	185 < $\sigma$ < 230	-0.1547	0.0079	3.3209
Mg b	230 < $\sigma$ < 325	-0.1443	0.0083	3.6861
C 4668	30 < $\sigma$ < 125	-0.4376	0.0354	4.4164
C 4668	125 < $\sigma$ < 185	-0.5219	0.0142	5.2554
C 4668	185 < $\sigma$ < 230	-0.3636	0.0124	6.1250
C 4668	230 < $\sigma$ < 325	-0.3249	0.0153	6.7582
Ca 4227	30 < $\sigma$ < 125	-0.0772	0.0315	1.4471
Ca 4227	125 < $\sigma$ < 185	-0.0834	0.0121	1.5851
Ca 4227	185 < $\sigma$ < 230	-0.0760	0.0104	1.6896
Ca 4227	230 < $\sigma$ < 325	-0.0658	0.0116	1.7962
Corrected H $\beta$	30 < $\sigma$ < 125	-0.0255	0.0260	2.1447
Corrected H $\beta$	125 < $\sigma$ < 185	0.0525	0.0109	2.0780
Corrected H $\beta$	185 < $\sigma$ < 230	0.0730	0.0102	1.9444
Corrected H $\beta$	230 < $\sigma$ < 325	0.0908	0.0115	1.7897
[Fe/H]	30 < $\sigma$ < 125	-0.0791	0.0163	-0.1343
[Fe/H]	125 < $\sigma$ < 185	-0.0545	0.0066	-0.0342
[Fe/H]	185 < $\sigma$ < 230	-0.0193	0.0044	0.0252
[Fe/H]	230 < $\sigma$ < 325	-0.0069	0.0042	0.0232
[Mg/Fe]	30 < $\sigma$ < 125	0.0694	0.0268	0.0359
[Mg/Fe]	125 < $\sigma$ < 185	-0.0051	0.0124	-0.0248
[Mg/Fe]	185 < $\sigma$ < 230	0.0071	0.0095	-0.0125
[Mg/Fe]	230 < $\sigma$ < 325	0.0154	0.0103	0.0143
[C/Fe]	30 < $\sigma$ < 125	-0.0107	0.0266	-0.0537
[C/Fe]	125 < $\sigma$ < 185	-0.0606	0.0156	-0.0056
[C/Fe]	185 < $\sigma$ < 230	0.0056	0.0109	0.1232
[C/Fe]	230 < $\sigma$ < 325	-0.0153	0.0079	0.2063

NOTE. — The calculated gradients for each measured metallicity indicator and the EZ\_Ages results for the data binned by velocity dispersion. The units are dex kpc<sup>-1</sup>.



TABLE 6  
GRADIENTS IN METALLICITY INDICATORS VERSUS SCALED RADIUS

Measure	$\sigma$ Range (km s <sup>-1</sup> )	Gradient	Uncertainty in Gradient	Value at 0.5 $R_e$
[MgFe]	30 < $\sigma$ < 125	-0.2322	0.0377	2.7716
[MgFe]	125 < $\sigma$ < 185	-0.4138	0.0221	3.0104
[MgFe]	185 < $\sigma$ < 230	-0.6042	0.0269	3.1210
[MgFe]	230 < $\sigma$ < 325	-0.7705	0.0399	3.2333
< Fe >	30 < $\sigma$ < 125	-0.2667	0.0629	2.6716
< Fe >	125 < $\sigma$ < 185	-0.3492	0.0370	2.8064
< Fe >	185 < $\sigma$ < 230	-0.5079	0.0435	2.8166
< Fe >	230 < $\sigma$ < 325	-0.5760	0.0630	2.8363
Mg b	30 < $\sigma$ < 125	-0.1845	0.0425	2.7957
Mg b	125 < $\sigma$ < 185	-0.4954	0.0253	3.1388
Mg b	185 < $\sigma$ < 230	-0.6881	0.0319	3.3636
Mg b	230 < $\sigma$ < 325	-0.9081	0.0480	3.5929
C 4668	30 < $\sigma$ < 125	-0.8821	0.0654	5.0693
C 4668	125 < $\sigma$ < 185	-1.5585	0.0384	5.7810
C 4668	185 < $\sigma$ < 230	-1.6801	0.0500	6.1940
C 4668	230 < $\sigma$ < 325	-2.1148	0.0888	6.5130
Ca 4227	30 < $\sigma$ < 125	-0.1371	0.0582	1.5715
Ca 4227	125 < $\sigma$ < 185	-0.2527	0.0327	1.6673
Ca 4227	185 < $\sigma$ < 230	-0.3539	0.0421	1.7027
Ca 4227	230 < $\sigma$ < 325	-0.4386	0.0675	1.7414
Corrected H $\beta$	30 < $\sigma$ < 125	-0.0446	0.0481	2.1860
Corrected H $\beta$	125 < $\sigma$ < 185	0.1457	0.0294	2.0196
Corrected H $\beta$	185 < $\sigma$ < 230	0.3013	0.0414	1.9126
Corrected H $\beta$	230 < $\sigma$ < 325	0.5337	0.0667	1.8296
[Fe/H]	30 < $\sigma$ < 125	-0.2311	0.0303	-0.0513
[Fe/H]	125 < $\sigma$ < 185	-0.0709	0.0151	0.0185
[Fe/H]	185 < $\sigma$ < 230	-0.1157	0.0176	-0.0040
[Fe/H]	230 < $\sigma$ < 325	-0.1740	0.0290	-0.0325
[Mg/Fe]	30 < $\sigma$ < 125	0.1363	0.0551	-0.0522
[Mg/Fe]	125 < $\sigma$ < 185	-0.0068	0.0377	-0.0474
[Mg/Fe]	185 < $\sigma$ < 230	0.1155	0.0411	-0.0038
[Mg/Fe]	230 < $\sigma$ < 325	0.0784	0.0567	0.0236
[C/Fe]	30 < $\sigma$ < 125	-0.1861	0.0517	0.0284
[C/Fe]	125 < $\sigma$ < 185	-0.2005	0.0419	0.0616
[C/Fe]	185 < $\sigma$ < 230	-0.0758	0.0575	0.1060
[C/Fe]	230 < $\sigma$ < 325	-0.1251	0.0710	0.1785

NOTE. — The calculated gradients for each measured metallicity indicator and the EZ\_Ages results binned by velocity dispersion. The units are dex.

TABLE 7  
LOGARITHMIC GRADIENTS: STELLAR MASS BINNING

Measure	$\log M$	$d(\text{Measure})/d \log r$	Error
[Fe/H]	$10.0 < \log(M) < 10.3$	-0.3028	0.0657
[Fe/H]	$10.3 < \log(M) < 10.7$	-0.0906	0.0296
[Fe/H]	$10.7 < \log(M) < 11.0$	-0.1709	0.0343
[Fe/H]	$11.0 < \log(M) < 11.5$	-0.1832	0.0702
[Mg/Fe]	$10.0 < \log(M) < 10.3$	0.1552	0.2066
[Mg/Fe]	$10.3 < \log(M) < 10.7$	-0.0075	0.1302
[Mg/Fe]	$10.7 < \log(M) < 11.0$	-0.0712	0.1519
[Mg/Fe]	$11.0 < \log(M) < 11.5$	0.0840	0.2212
[C/Fe]	$10.0 < \log(M) < 10.3$	-0.2294	0.1886
[C/Fe]	$10.3 < \log(M) < 10.7$	-0.2204	0.1292
[C/Fe]	$10.7 < \log(M) < 11.0$	-0.0803	0.1836
[C/Fe]	$11.0 < \log(M) < 11.5$	-0.2851	0.2300

NOTE. — The calculated logarithmic gradients for the metallicity and  $[\alpha/\text{Fe}]$  ratios for all four stellar mass bins.

TABLE 8  
LOGARITHMIC GRADIENTS: VELOCITY DISPERSION BINNING

Measure	$\sigma$	$d(\text{Measure})/d \log r$	Error
[Fe/H]	$30 < \sigma < 125$	-0.3069	0.0853
[Fe/H]	$125 < \sigma < 185$	-0.0708	0.0343
[Fe/H]	$185 < \sigma < 230$	-0.1203	0.0403
[Fe/H]	$230 < \sigma < 325$	-0.1866	0.0776
[Mg/Fe]	$30 < \sigma < 125$	0.1810	0.2223
[Mg/Fe]	$125 < \sigma < 185$	-0.0068	0.1312
[Mg/Fe]	$185 < \sigma < 230$	0.1201	0.1250
[Mg/Fe]	$230 < \sigma < 325$	0.0840	0.2212
[C/Fe]	$30 < \sigma < 125$	-0.2472	0.1957
[C/Fe]	$125 < \sigma < 185$	-0.2005	0.1293
[C/Fe]	$185 < \sigma < 230$	-0.0788	0.1791
[C/Fe]	$230 < \sigma < 325$	-0.1341	0.2528

NOTE. — The calculated logarithmic gradients for the metallicity and  $[\alpha/\text{Fe}]$  ratios for all four velocity dispersion bins.

## REFERENCES

- Abazajian, K. N., Adelman-McCarthy, J. K., Agüeros, M. A., Allam, S. S., Allende Prieto, C., An, D., Anderson, K. S. J., Anderson, S. F., Annis, J., Bahcall, N. A., & et al. 2009, *ApJS*, 182, 543
- Blanton, M. R., Kazin, E., Muna, D., Weaver, B. A., & Price-Whelan, A. 2011, *AJ*, 142, 31
- Blanton, M. R. & Moustakas, J. 2009, *ARA&A*, 47, 159
- Blanton, M. R. & Roweis, S. 2007, *AJ*, 133, 734
- Blanton, M. R., Schlegel, D. J., Strauss, M. A., Brinkmann, J., Finkbeiner, D., Fukugita, M., Gunn, J. E., Hogg, D. W., Ivezić, Ž., Knapp, G. R., Lupton, R. H., Munn, J. A., Schneider, D. P., Tegmark, M., & Zehavi, I. 2005, *AJ*, 129, 2562
- Bundy, K., Bershady, M. A., Law, D. R., Yan, R., Drory, N., MacDonald, N., Wake, D. A., Cherinka, B., Sánchez-Gallego, J. R., Weijmans, A.-M., Thomas, D., Tremonti, C., Masters, K., Coccatto, L., Diamond-Stanic, A. M., Aragón-Salamanca, A., Avila-Reese, V., Badenes, C., Falcón-Barroso, J., Belfiore, F., Bizyaev, D., Blanc, G. A., Bland-Hawthorn, J., Blanton, M. R., Brownstein, J. R., Byler, N., Cappellari, M., Conroy, C., Dutton, A. A., Emsellem, E., Etherington, J., Frinchaboy, P. M., Fu, H., Gunn, J. E., Harding, P., Johnston, E. J., Kauffmann, G., Kinemuchi, K., Klaene, M. A., Knapen, J. H., Leauthaud, A., Li, C., Lin, L., Maiolino, R., Malanushenko, V., Malanushenko, E., Mao, S., Maraston, C., McDermid, R. M., Merrifield, M. R., Nichol, R. C., Oravetz, D., Pan, K., Parejko, J. K., Sanchez, S. F., Schlegel, D., Simmons, A., Steele, O., Steinmetz, M., Thanjavur, K., Thompson, B. A., Tinker, J. L., van den Bosch, R. C. E., Westfall, K. B., Wilkinson, D., Wright, S., Xiao, T., & Zhang, K. 2015, *ApJ*, 798, 7
- Carollo, C. M., Danziger, I. J., & Buson, L. 1993, *MNRAS*, 265, 553
- Chiosi, C., Merlin, E., & Piovan, L. 2012, *ArXiv e-prints*
- Conroy, C. & Gunn, J. E. 2010, *ApJ*, 712, 833
- Conroy, C., Gunn, J. E., & White, M. 2009, *ApJ*, 699, 486
- Couture, J. & Hardy, E. 1988, *JRASC*, 82, 277
- Di Matteo, P., Pipino, A., Lehnert, M. D., Combes, F., & Semelin, B. 2009, *A&A*, 499, 427
- Faber, S. M., Friel, E. D., Burstein, D., & Gaskell, C. M. 1985, *ApJS*, 57, 711
- Gonzalez, J. J. & Gorgas, J. 1995, in *Astronomical Society of the Pacific Conference Series*, Vol. 86, *Fresh Views of Elliptical Galaxies*, ed. A. Buzzoni, A. Renzini, & A. Serrano, 225
- González Delgado, R. M., García-Benito, R., Pérez, E., Cid Fernandes, R., de Amorim, A. L., Cortijo-Ferrero, C., Lacerda, E. A. D., López Fernández, R., Sánchez, S. F., Vale Asari, N., & CALIFA collaboration. 2014, *ArXiv e-prints*
- Graves, G. J. & Schiavon, R. P. 2008, *ApJS*, 177, 446
- Greene, J. E., Murphy, J. D., Graves, G. J., Gunn, J. E., Raskutti, S., Comerford, J. M., & Gebhardt, K. 2013, *ApJ*, 776, 64
- Hopkins, P. F., Cox, T. J., Dutta, S. N., Hernquist, L., Kormendy, J., & Lauer, T. R. 2009, *ApJS*, 181, 135
- Kawata, D. & Gibson, B. K. 2003, *MNRAS*, 340, 908
- Kobayashi, C. 2003, *Ap&SS*, 284, 853
- Koleva, M., Prugniel, P., de Rijcke, S., & Zeilinger, W. W. 2011, *MNRAS*, 417, 1643
- Kuntschner, H., Emsellem, E., Bacon, R., Cappellari, M., Davies, R. L., de Zeeuw, P. T., Falcón-Barroso, J., Krajnović, D., McDermid, R. M., Peletier, R. F., Sarzi, M., Shapiro, K. L., van den Bosch, R. C. E., & van de Ven, G. 2010, *MNRAS*, 408, 97
- Martinelli, A., Matteucci, F., & Colafrancesco, S. 1998, *MNRAS*, 298, 42
- Mehlert, D., Saglia, R. P., Bender, R., & Wegner, G. 2000, *A&AS*, 141, 449
- Mehlert, D., Thomas, D., Saglia, R. P., Bender, R., & Wegner, G. 2003, *A&A*, 407, 423
- Munn, J. A. 1992, *ApJ*, 399, 444
- Ogando, R. L. C., Maia, M. A. G., Chiappini, C., Pellegrini, P. S., Schiavon, R. P., & da Costa, L. N. 2005, *ApJ*, 632, L61
- Ogando, R. L. C., Maia, M. A. G., Chiappini, C., Pellegrini, P. S. S., Schiavon, R. P., & da Costa, L. N. 2006, in *Revista Mexicana de Astronomía y Astrofísica Conference Series*, Vol. 26, *Revista Mexicana de Astronomía y Astrofísica Conference Series*, 119–120
- Pastorello, N., Forbes, D. A., Foster, C., Brodie, J. P., Usher, C., Romanowsky, A. J., Strader, J., & Arnold, J. A. 2014, *ArXiv e-prints*
- Pipino, A., D’Ercole, A., Chiappini, C., & Matteucci, F. 2010, *MNRAS*, 407, 1347
- Rawle, T. D., Smith, R. J., & Lucey, J. R. 2010, *MNRAS*, 401, 852
- Rawle, T. D., Smith, R. J., Lucey, J. R., & Swinbank, A. M. 2008, *MNRAS*, 389, 1891
- Schiavon, R. P. 2007, *ApJS*, 171, 146
- Shen, S., Mo, H. J., White, S. D. M., Blanton, M. R., Kauffmann, G., Voges, W., Brinkmann, J., & Csabai, I. 2003, *MNRAS*, 343, 978
- Spolaor, M., Kobayashi, C., Forbes, D. A., Couch, W. J., & Hau, G. K. T. 2010, *MNRAS*, 408, 272
- Strauss, M. A., Weinberg, D. H., Lupton, R. H., Narayanan, V. K., Annis, J., Bernardi, M., Blanton, M., Burles, S., Connolly, A. J., Dalcanton, J., Doi, M., Eisenstein, D., Frieman, J. A., Fukugita, M., Gunn, J. E., Ivezić, Ž., Kent, S., Kim, R. S. J., Knapp, G. R., Kron, R. G., Munn, J. A., Newberg, H. J., Nichol, R. C., Okamura, S., Quinn, T. R., Richmond, M. W., Schlegel, D. J., Shimasaku, K., SubbaRao, M., Szalay, A. S., Vanden Berk, D., Vogeley, M. S., Yanny, B., Yasuda, N., York, D. G., & Zehavi, I. 2002, *AJ*, 124, 1810
- Thomas, D., Maraston, C., & Bender, R. 2003, *MNRAS*, 339, 897
- Trager, S. C., Faber, S. M., Worthey, G., & González, J. J. 2000, *AJ*, 119, 1645
- Yan, R. & Blanton, M. R. 2012, *ApJ*, 747, 61
- Yan, R., Newman, J. A., Faber, S. M., Konidaris, N., Koo, D., & Davis, M. 2006, *ApJ*, 648, 281
- Yuan, T.-T., Kewley, L. J., & Rich, J. 2013, *ApJ*, 767, 106
- Zhu, G., Blanton, M. R., & Moustakas, J. 2010, *ApJ*, 722, 491